Observations of particle size distributions of single crystal and
aggregate frozen hydrometeors

By

Manuel "Marty" Martinez

Thesis

submitted to the Faculty of the

Graduate School of Vanderbilt University

in partial fulfillment of the requirements

for the degree of

MASTER OF SCIENCE
in
Earth and Environmental Sciences

August, 2015

Nashville, Tennessee

Approved:

Ralf Bennartz, Ph.D.
David Jon Furbish, Ph.D.

ACKNOWLEDGEMENTS

TABLE OF CONTENTS

Page

Chapter

LIST OF FIGURES

LIST OF TABLES

CHAPTER 1

Introduction

Together the Antarctic and Greenland ice sheets (AIS and GrIS respectively) are the largest source of freshwater on the planet. The two ice sheets are among the principal contributors to sea level rise and they contain ice with the capacity to raise the global sea level 70 meters [*van den Broeke et al.,* 2011]. Over the past two decades GrIS mass loss has contributed an estimated eight millimeters to sea level rise, corresponding to almost 3000 Gigatonnes of mass loss [*Vaughan et al.,* 2013](Figure 1). Ice sheet mass balance (MB) is heuristically defined in the following equations [*van den Broeke et al.,* 2009]:

$$(1) \qquad MB = \frac{dM}{dt} = SMB - D$$

where the rate of change of mass ($\frac{dM}{dt}$) is defined as the difference between surface mass balance (SMB [Gt yr^{-1}]) and the ice discharge (D). SMB is a value determined by the contribution of processes involved in accumulation and ablation.

$$(2) \qquad SMB = Snow + Rain - Sublimation - Runoff$$
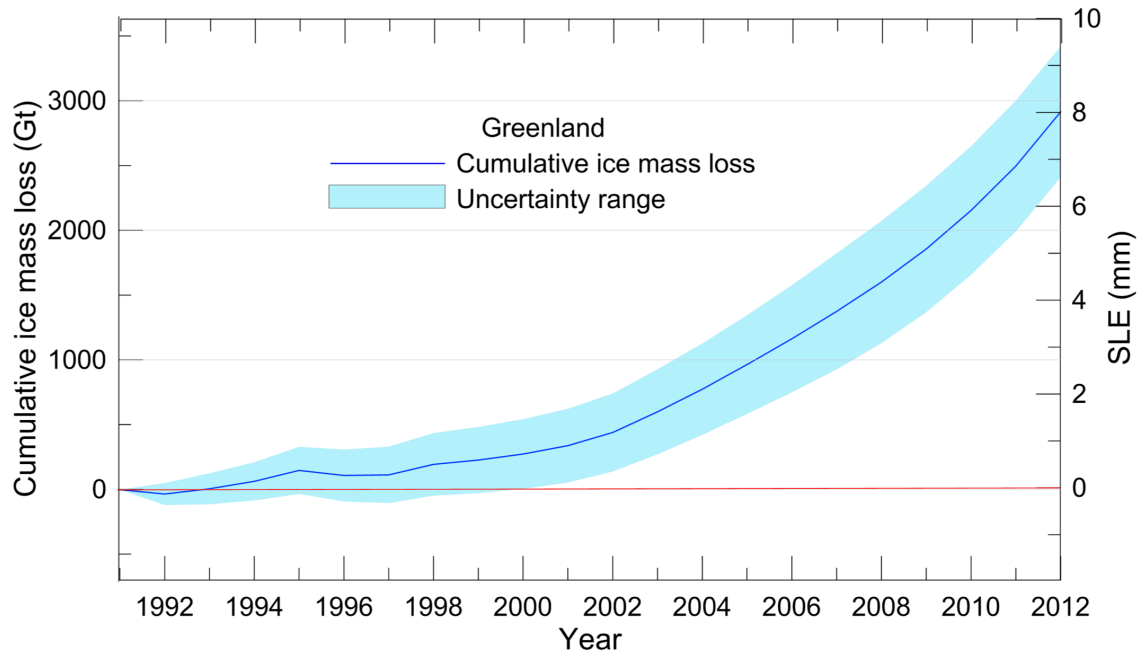
Figure 1 shows combined results for two decades from 18 studies that estimate the mass balance of the Greenland ice sheet. The increasing uncertainty band reflects the high density of studies rather than a decrease in physical knowledge over time [*Vaughan et al.*, 2013].

Remote sensing methods for estimating mass balance gather physical measurements that approximate mass flux from individual processes defined in (2). Three independent techniques, altimetry, gravity-change, and the mass budget method [*Ewert et al.*, 2012; *Rignot et al.*, 2011], measure dynamic properties of ice sheets in an effort to quantify the mass balance. Researchers using the altimetry approach [*Howat et al.*, 2011; *Krabill et al.*, 2004; *Pritchard et al.*, 2009; *Rignot et al.*, 2008] employ satellite sensors to measure changes in surface elevation of an ice sheet over time and calculate the effective volume and mass changes. Error associated with this method is due the lack of accurate mass-shape relationships, which lead to incorrect assumptions for the spatial variation of ice density throughout the sheet. As a metric for the magnitude of uncertainty, *Pritchard et al.* [2009] presented calculated volumetric glacier discharge from an altimetry study

that contain a range of uncertainties from 10 to 60 %.   Recent studies address this source of error by simultaneously measuring changes in gravity in order to verify ice density variability [*Sasgen et al.*, 2012].

Independently, the gravity-change method estimates changes in mass from temporal fluctuations of gravity. If we assume that most of the interior is approximately homogeneous, then spatial variations in the strength of Earth's gravitational field exist due to density differences of material in the lithosphere (on average the top 50 km of crust and mantle). Processes associated with point measurements of gravity anomalies are difficult to ascertain, because the strength of the field is affected by a vertical profile of material between the instrument and the center of Earth's mass. By considering a vertical profile as one point on the surface of a sphere (Earth), we mask the vertical location of a density anomaly source. Nevertheless, ice sheet gravimetry studies became more feasible with the launch of the twin satellites, collectively referred to as GRACE (Gravity Recovery and Climate Experiment), that function to detect gravity anomalies as they orbit Earth at 15 revolutions per day [*Ewert et al.*, 2012; *Rignot et al.*, 2011; *Sasgen et al.*, 2012; *van den Broeke et al.*, 2009]. Despite the increase in data availability, studies using gravimetry to calculate mass loss rates (Table 1) do not agree with each other. Measureable changes in elevation and density (gravity) are affected greatly by precipitation and the associated accumulation, yet neither method is able to independently quantify the impact of these processes. Therefore precipitation measurement techniques from our research will have the greatest impact when applied to calculations of mass balance using the mass budget method.

Author	Method/sensor	GRACE solution	Period	Trend	
				Volume [km^3 yr^{-1}]	Mass [Gt yr^{-1}]
Krabill et al. (2000)[†]	Airborne LA		06/94–05/99	−51	
Zwally et al. (2005)[†]	ERS1/2		04/92–10/02		+11 ± 03
Slobbe et al. (2009)[†]	ICESat		02/03–04/07		−139 ± 68
Rignot and Kanagaratnam (2006)[‡]	InSAR		2005	−224 ± 41	
Chen et al. (2006)*	GRACE	CSR	04/02–11/05		−219 ± 21
Ramillien et al. (2006)*	GRACE	CNES	07/02–03/05		−118 ± 14
Luthcke et al. (2006)*	GRACE	Mascon	01/03–12/05		−101 ± 16
Wouters et al. (2008)*	GRACE	CSR	02/03–01/08		−179 ± 25
Velicogna (2009)*	GRACE	CSR	04/02–02/09		−230 ± 33
Slobbe et al. (2009)*	GRACE	CSR	04/02–06/07		−218 ± 18
Slobbe et al. (2009)*	GRACE	GFZ	08/02–06/07		−168 ± 05
Present study[†]	ICESat		09/03–03/08	−205 ± 11	−185 ± 28
Present study*	GRACE	GFZ	08/02–06/09		−191 ± 21

Table 1 shows results of selected mass balance studies over the past twenty years. This collection of estimates shows the level of uncertainty between studies is high even for studies that obtain the same data sets for the same periods in time [*Ewert et al.*, 2012].

In order to consider contributions from the processes in (1), the mass budget method combines data sets from multiple instruments on either side of the ice sheet 'grounding line' [*Rignot et al.*, 2011]. This line defines the boundary between the media (solid rock or ocean water) that make contact with the bottom of the ice sheet. The mass contribution direction (increase or decrease) for associated processes depends on the location with respect to the 'grounding line'; processes that add mass are classified under surface mass balance (SMB) processes, while ice sheet discharge processes detract mass from the system. Despite the process inclusive nature of this method, SMB calculations have standard errors of up to 24% of the average SMB (417 Gt year^{-1}) [*van den Broeke et al.*, 2011]. By increasing the accuracy of frozen precipitation measurement, the measurement algorithms proposed in this research have the potential to be used to increase our knowledge of the global SLR contribution due to ice sheet mass loss.

Current measurement methods of frozen precipitation contain variable uncertainty and the inability to distinguish microphysical properties of snowflakes en masse contributes to the error [*Kulie et al.*, 2013]. Properties of individual ice particles, such as habit and density, vary as functions of relative humidity,

temperature, presence of convection, and other atmospheric conditions that fluctuate over time and space. Spatially extensive snowfall data collection is simplified by remote sensing; in particular recent studies examine the response of radar reflectivity to frozen precipitation [*Kneifel et al.*, 2011; *Kulie et al.*, 2010; *Nowell et al.*, 2013]. The most advanced techniques measure scattering properties of frozen hydrometeors at different wavelengths. By comparing reflectance profiles at these wavelengths, the studies attempt to determine the impact of particle size, shape-mass relationships, and other microphysical properties on radar reflectance to increase the accuracy of snow mass measurements.

Radar retrieval methods for frozen precipitation were originally adopted from successful techniques developed to study liquid precipitation. Mass-Diameter relationships for rain droplets are physically straightforward due to the nearly spherical, constant density nature of the drops [*Seliga and Bringi*, 1976]. Scientists working with rainfall measurement use forward modeling methods to determine particle volume from radar reflectivity based on robust data relating Rayleigh scattering to particle size distributions (PSD, Section 4). These distributions are defined as the expected concentration of particles within a given volume of air versus liquid equivalent diameter and they are always plotted on semi-log axes in order to make exponential distributions visually distinguishable.

Forward modeling techniques have also been applied to snowfall measurements. The consistency of droplet shape allows accurate determination of liquid precipitation mass; however *Kajikawa and Heymsfield* [1989] observed that a majority of snowflakes are irregular aggregates. Forward modeling of reflectivity

signatures from snowflakes using the methods developed for liquid precipitation oversimplify particle irregularity to spheroids in scattering calculations, which contributes to an estimated 50-75% error in snowfall mass measurement accuracy [*Kneifel et al.*, 2011]. The development of snowflake measurement, presented by *Nowell et al.* [2013], has led to two classes of shape simplification: irregular aggregates and non-aggregates (broadly referred to as aggregation state). There are two dominant growth processes that define ice particle aggregation state, diffusion and aggregation. Information connecting the impact of growth processes on PSD shape is presented in chapter 4.

Our goal is to use the MASC (Multi-Angle Snowflake Camera)[*Garrett et al.*, 2012], a remote sensing instrument, to measure and record two-dimensional particle information simultaneously from three different positions about the same vertical axis. We have developed autonomous software to process image triplets from the MASC and return physical measurements of snowflakes throughout a precipitation event. We believe that the aforementioned growth processes should influence the shape of particle size distributions and focus our research into a three-pronged hypothesis:

- Measurements of falling snow near ground level will produce a distribution that is not simply exponential, but a combination of shapes that depend on aggregation state distributions
- Non-aggregate particles will follow a log-normal distribution
- Aggregation creates enough large particles to populate an exponential distribution.

The remainder of this work is structured as follows: chapter 2 contains information about the MASC, the analysis software that we developed, and laboratory experiments conducted to learn about the MASC. Chapter 3 displays information gathered from our laboratory experiments used in snowflake analysis. Physical evidence that supports our hypothesis is provided via explanation of particle microphysics in chapter 4. The 5th chapter breaks our results into 3 parts: particle segregation, the impact of aggregation state on particle size distribution shape, and comparing our results to accepted publications. Finally, conclusions and future work are presented in chapter 6.

CHAPTER 2

Instruments and Methods

2.1 The MASC

In the Multi-Angle Snowflake Camera, three cameras are positioned in the same horizontal plane each separated by a 36° rotation about the center, like edges of a decagon [*Garrett et al.*, 2012]. The MASC collects three images simultaneously; each image is a projection of the three-dimensional optical field. The MASC software is designed to collect large data sets of ice particles in a short amount of time. Prior to development of the MASC, snowflake image measurements were done individually using a time consuming and labor-intensive process. The use of infrared (IR) sensors to detect falling objects and trigger the cameras minimizes user interaction required for data acquisition. Figure 2 is a top down schematic of the MASC; particles that fall through the ring near point D trigger the cameras (A, B, and C). The images record information of snowflakes in the visible spectrum, which we use to identify local size distribution of snowflakes during a precipitation event. The automated capture creates easily obtainable, very large data sets; one event (3-4 hours long) in Boulder, CO produced over three thousand image triplets.

19.42 cm

6 cm

18.47 cm

9.88 cm

y

D

x

A

B

C
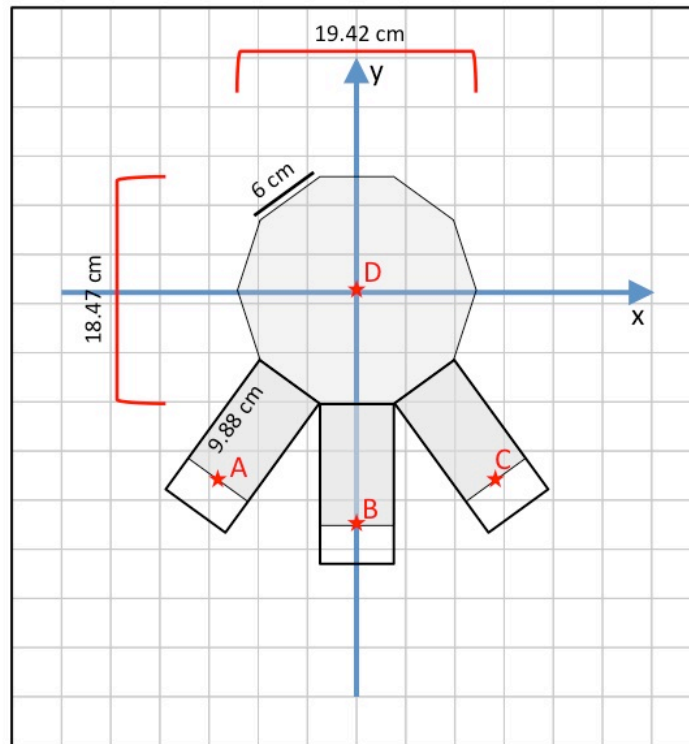
Center of focal plane
All values in cm

A	:	[-11.23,	-15.46]
B	:	[0.00,	-19.11]
C	:	[+11.23,	+15.46]
D	:	[0.00,	0.00]

AD = BD = CD = 19.11 cm

Figure 2. Top down schematic of the MASC. Points A,B,and C are cameras and point D is the center of the IR detection zone. The infrared detectors are located on the decagon edges directly above (positive direction on y-axis) the x-axis on either side of the MASC ring.

2.2 Data analysis methods

If triggered at maximum frequency (2 Hz), the MASC is capable of collecting

up to 7200 image triplets in an hour. The magnitude of these data sets motivated

me to create autonomous software for individual particle measurement. Our goal is

to isolate and identify the snowflake responsible for triggering the MASC (hereby referred to as the 'trigger flake') within all three cameras and record two-dimensional measurements of each snowflake. Figure 3 outlines that process in principal.

The MASC software assigns a sequential "tag" to each image triplet; the tag, date, and time are embedded in the filename (and used to match image triplets). It is important to note that the software is designed so the user can use any function independently on an individual MASC image; therefore each image in a triplet is processed separately. By applying IDL's LABEL_REGION function, we can isolate pixels that belong to the same snowflake and create a separate image for each flake. Raw image coordinates of isolated snowflakes are used to narrow the search for the trigger flake by excluding flakes outside of the two-dimensional trigger zone (represented by the red band in Figure 3.B). Accepted snowflakes have their images sent to a function that measures and stores physical information in identical data structures.

The first item in the structure (*flake_img)* is an 800x800 pixel image of the snowflake centered at [400,400]. The next four parameters are linear measurements of the particle in pixels; *x_width* and *y_width* are the maximum horizontal and vertical dimensions of the particle. *rmax* corresponds to the semi-major axis of an ellipse and is measured as the absolute maximum one-dimensional measurement of the particle while *rmin* (semi-minor axis)is the largest width of the particle when measured perpendicular to the direction of *rmax*. *ASR* is the aspect ratio, which we define as the ratio between *rmin* and *rmax*. *ARR* is the area ratio,

defined as the ratio between pixels within a snowflake and pixels within the snowflake's circumscribing circle (diameter = *rmax*). *Angle* is the orientation of *rmax* measured in degrees counter-clockwise from horizontal. *x_off* and *y_off* are the horizontal and vertical pixel coordinates of the snowflake within the raw image. *Sharpness* is a ratio that is used to determine how in focus a particle is, we will explicitly define this parameter later in the section. The last item in the structure (*fname*) is a string containing the file name of the raw image that contains the snowflake.

When an image contains multiple snowflakes within the trigger zone (Figure 3.C) we use the *sharpness* parameter to quantify the focus of each snowflake and isolate which snowflake triggered the MASC. The edge of an out-of-focus particle is characterized by a 'fuzzy' boundary created by a shallow gradient of gray-scale brightness values instead of a sharp contrast between brightness values of the particle and black background. The Sobel-filter is an image-processing tool that approximates brightness gradients across images; Figure 4(sobel+raw) displays 4 raw snowflake images juxtaposed with their sobel filtered images. We define *sharpness* as the ratio between the sum of all pixels in a Sobel-filtered image and the sum of all pixels in an un-altered image. Within the software flowchart (Figure 3.D), we segregate some snowflakes by their *sharpness* to give readers a sense of magnitude for this parameter. The software ranks snowflakes from the same image by their sharpness value and chooses the highest rank as the trigger flake. The snowflake software processed 2540 unique image triplets from the Boulder deployment, but only 60% of these triplets were used. (Table 2) The software
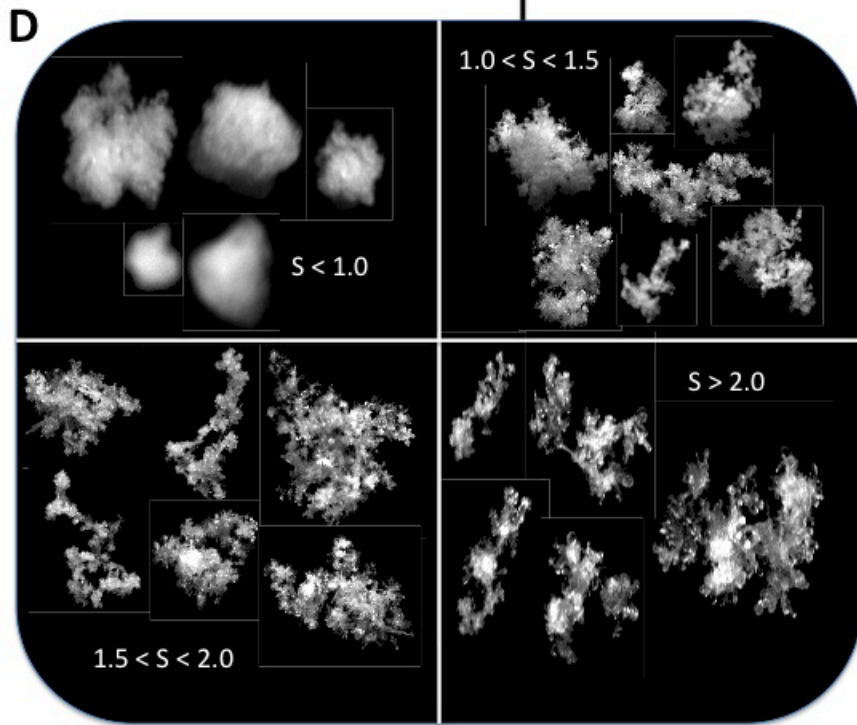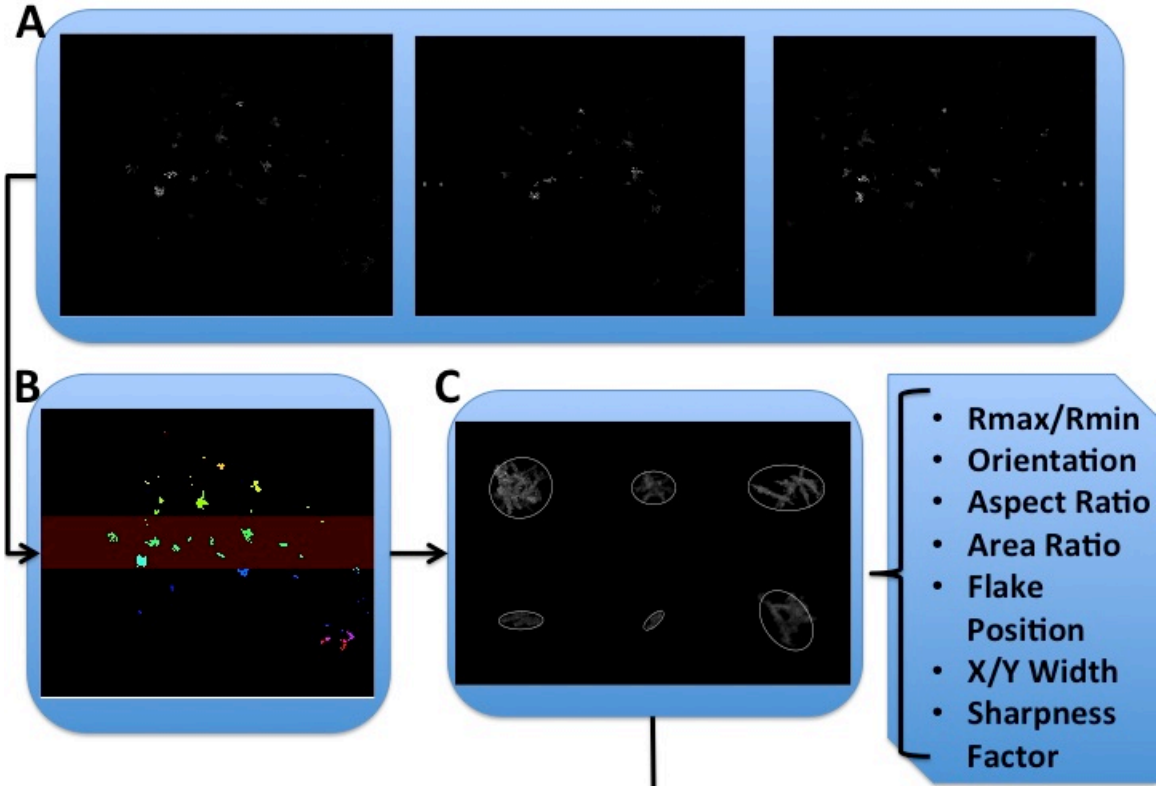
design ignores images when there are no snowflakes in the trigger zone (Figure 3.B) or when snowflake brightness is too low to resolve well. This failsafe was implemented to maintain autonomy during processing. Software accuracy of 88% was determined by visual inspection of 3 snowflake images from each triplet.

After processing the images collected from Boulder, we need to convert maximum linear dimension (*Rmax)* into liquid water equivalent diameter (D_{LE}). Previous research present snowflake measurements with this property in order to reduce variation due to slight changes in atmospheric conditions. Conceptually D_{LE} is the diameter of a sphere of liquid water created by melting a snowflake, therefore this property is closely connected to mass and is not affected by variable density in particle crystal structure. The mass of a snowflake has been empirically connected to *Rmax* and D_{LE} is calculated by the mass-volume relationship of a sphere of water:

(3)
$$Mass_{est} \approx 0.022 * R\text{max}^{2.1}$$

(4)
$$D_{LE} = (\frac{6 * Mass_{est}}{\pi * \rho_w})^{\frac{1}{3}}$$

A

B

C

- Rmax/Rmin
- Orientation
- Aspect Ratio
- Area Ratio
- Flake Position
- X/Y Width
- Sharpness Factor

D

1.0 < S < 1.5

S < 1.0

S > 2.0

1.5 < S < 2.0

Figure 3 is a schematic flowchart designed to give readers an understanding of the snowflake software processes/algorithm. Starting with an image triplet (A) from the MASC, the software isolates and identifies snowflakes within the red trigger zone in section B. Physical measurements of each particle are calculated and used to determine which snowflake triggered the cameras. The sharpness factor is the primary parameter used in selecting this snowflake, and section D of this figure show 4 set of particles separated by sharpness values.
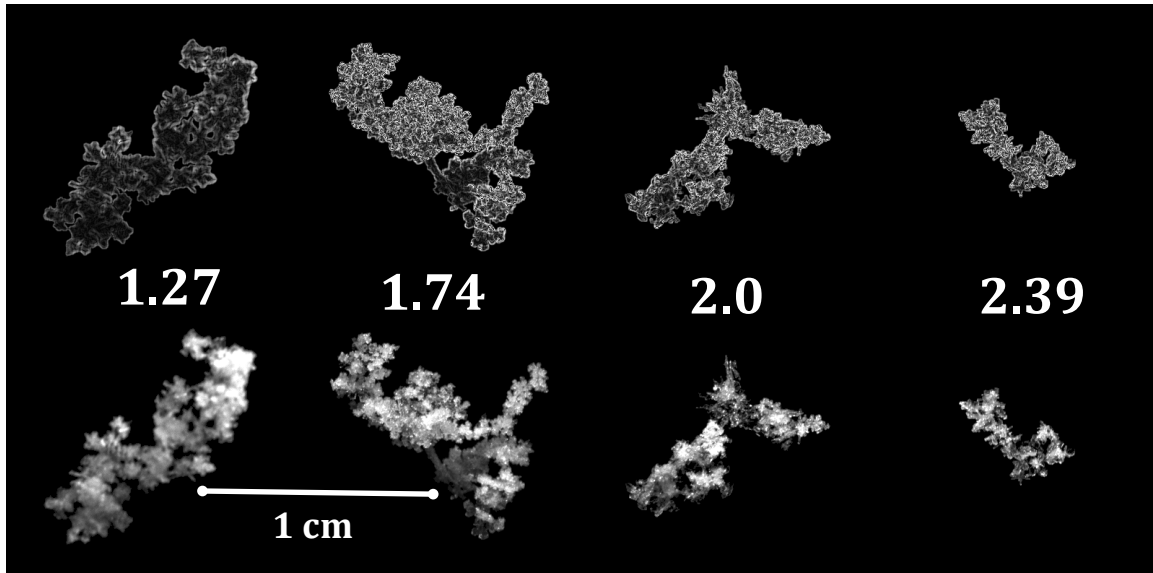
Figure 4. Adding all pixel values within the top images (sobel filtered) and dividing by the sum of pixels in the bottom images (raw) calculate the sharpness factor. Values greater than 1.0 are correlated with snowflakes that are in focus. Our theory is that fuzzy images will show less contrast between pixels within the snowflake, which corresponds to a darker (or lower valued) sobel filtered image. Dividing by the sum of pixels in the raw image will normalize extreme values collected in the sobel images.

Total Image Triplets	Discarded Triplets	Triplets Analyzed	Software Correctly Identified 3 Flakes	Software Accuracy
2540	1016	1524	1342	88%

**Table 2** is organized to display accuracy results of the snowflake software.

2.3 Laboratory experiments

In the laboratory we are able to measure and control the size and shape of objects captured by the MASC. Therefore, we designed experiments to create datasets used to give us more information about the instrument behavior in unique

situations. The following experiments contribute more to understanding the instrument than our research goals, and as such the presented details are intentionally succinct. Early experiments used a suspended water bottle and programmable valve to release droplets of an ink and water solution; during this phase we were testing how often the IR trigger system failed while also collecting image triplets of water spheroids. In another set of experiments, we dropped a ball bearing of known dimensions through the MASC camera ring and recorded information from the raw images. These experiments were used to define important parameters in the analysis software, and are explained in chapter 3. To learn about MASC susceptibility to missing information from irregularly shaped particles, we created and imaged objects from modeling clay and interconnected gears. In these experiments, we wanted to see how different each particle looks between the three cameras and how this can contribute to measurement error with the MASC.

2.4 The Boulder deployment

On March 17, 2014 we set up the MASC in Boulder, Colorado at the NCAR (National Center for Atmospheric Research) Marshall field site. The instrument was stationed a few meters from a trailer and tethered to the ground with guy-wires. Data cables ran from the MASC to computers inside the trailer where images were stored. We captured around 2700 image triplets over two snowfall events (March 28 and April 2-3) and the MASC was removed on April 24, 2014. Figure __ contains hourly temperature profiles plotted with a histogram showing the number of times the cameras were triggered.
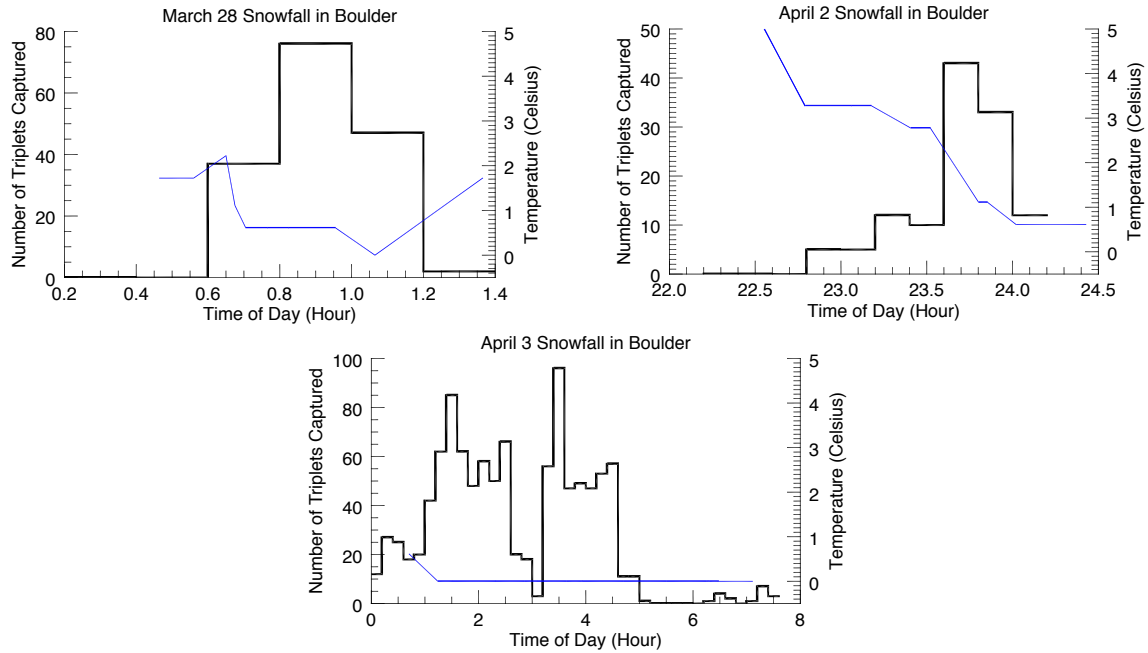
Figure 5 shows histograms of captured images (left axis) over time for the MASC. Over-plotted on each diagram is the temperature (right axis) recorded during snowfall. We can see that most images were captured early during April 3.

CHAPTER 3

Sensitivity Studies

3.1 Vertical trigger zone

Preliminary experiments were conducted by releasing a single 9525 um diameter ball-bearing 44 times over the center of the MASC to characterize its physical limitations. Spatial extent of the vertical trigger zone (different from the top down trigger zone) was defined by locating the vertical position of the ball-bearing center within each image collected. The histogram in Figure 6 relates vertical location of the ball-bearing to the IR diodes, we expect that trigger particles will be located within a predictable band on each MASC image.
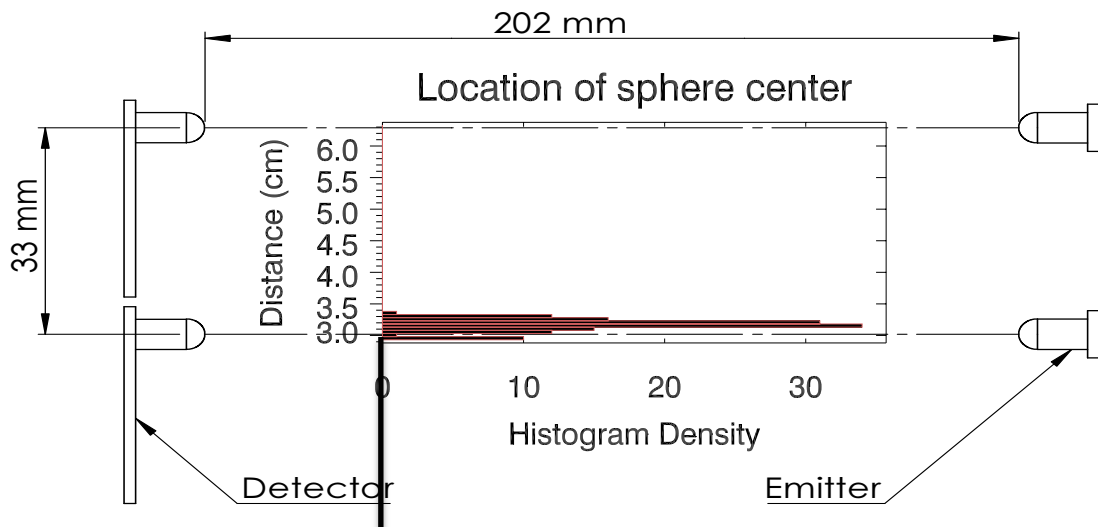

Figure 6. Histogram: ball-bearing vertical position within MASC image. IR diode schematic included to give spatial perspective of the vertical trigger zone. We were able to determine the vertical location of the IR diodes because they appear in the edges of images from the outside cameras.

3.2 Image resolution

Pixel resolution of the MASC was then addressed by measuring the ball

bearing within each using the snowflake measurement software. We record the

largest measurable diameter in pixels and assume that this diameter must be less

than or equal to the ball bearing diameter due to the object's spherical shape. The

histograms in Figure 7.A,B,C show the variability of measurements between the

three cameras of the MASC.

Histograms of Sphere Diameter
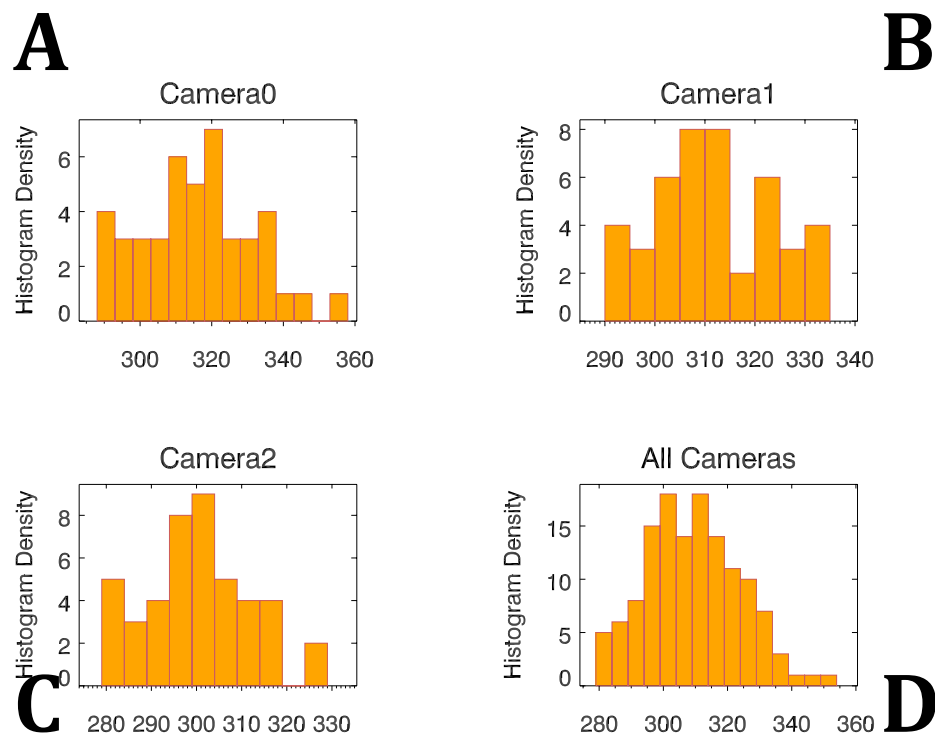
Figure 7. Histograms used to define pixel resolution where bins are measured ball bearing diameter in pixels. We combine the 3 distributions together because our software is designed to process each image regardless of position.

The final histogram (Figure 7.D) presents a measured diameter mean and

standard deviation of 309 and 14.6 pixels respectively. A resolution of 30.8252
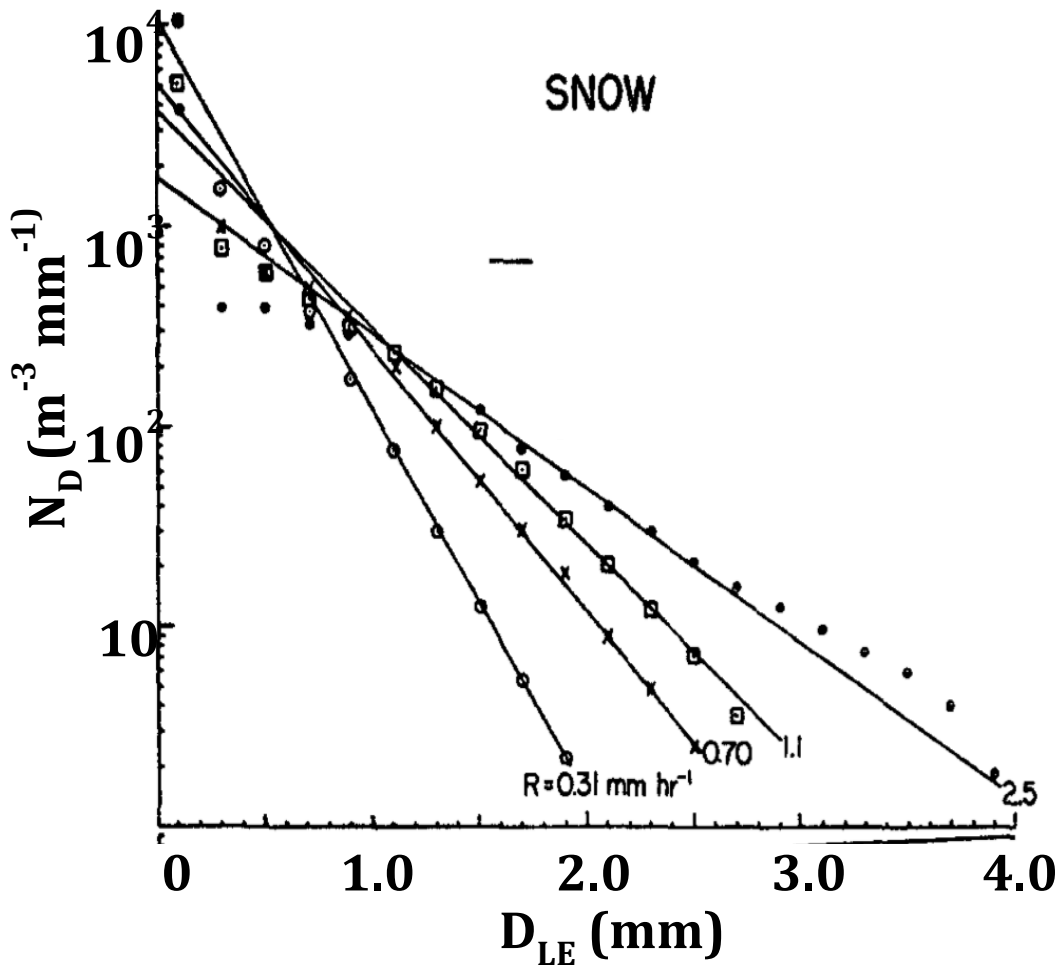
um/pixel is determined by dividing the actual diameter (9525 um) by the mean

measured diameter.

CHAPTER 4

Precipitation Microphysics

4.1 Particle Size Distributions

Figure 8 is the seminal particle size distribution for aggregate snowflakes[*Gunn and Marshall*, 1958]. The distributions are plotted on semi-log axes, which is why the exponential distributions appear to have linear relationships.

The first PSD was presented for liquid precipitation by *Marshall and Palmer* [1948] and studies with frozen precipitation then adopted the same method of presentation starting with *Gunn and Marshall* [1958] (Figure 8). As mentioned

previously, these distributions are plotted on semi-log axes because exponential

distributions appear as straight lines. *Sekhon and Srivastava* [1970] empirically

defined the following relationship for PSDs for snow that vary based on

precipitation rate (R):

$$(5) \qquad\qquad N_D = N_0 e^{-\Lambda D_{LE}}$$

$$(6) \qquad\qquad N_0 (m^{-3} mm^{-1}) = 3.8 x 10^3 R^{-0.87}$$

$$(7) \qquad\qquad \Lambda (cm^{-1}) = 25.5 R^{-0.48}$$

$$(8) \qquad\qquad D_0 (cm) = 0.144 R^{0.48}$$

where N_D is the number of particles expected at a given size within a volume

of air. D_{LE} is the liquid equivalent diameter of a particle, while Λ is an empirical

parameter that is defined only by precipitation rate.

An underlying exponential distribution has important implications for

particle observations. When the number of observations is high enough, we expect

to see most particles smaller than the mean recorded value. As particle size

increases past the mean particle count should decrease dramatically and we may

see gaps where no particles of a given size are recorded. The following subsection

provides physical evidence that suggests an exponential distribution may not fully

describe snowfall PSDs.

4.2 Precipitation processes

Information about the processes controlling ice particle growth gives a

physical justification for our hypotheses. The snowflakes captured during the

Boulder deployment exhibit evidence of three distinct growth processes: diffusion,

riming, and aggregation. The schematic below (Figure 9) provides visual

compliments to the following growth process descriptions.
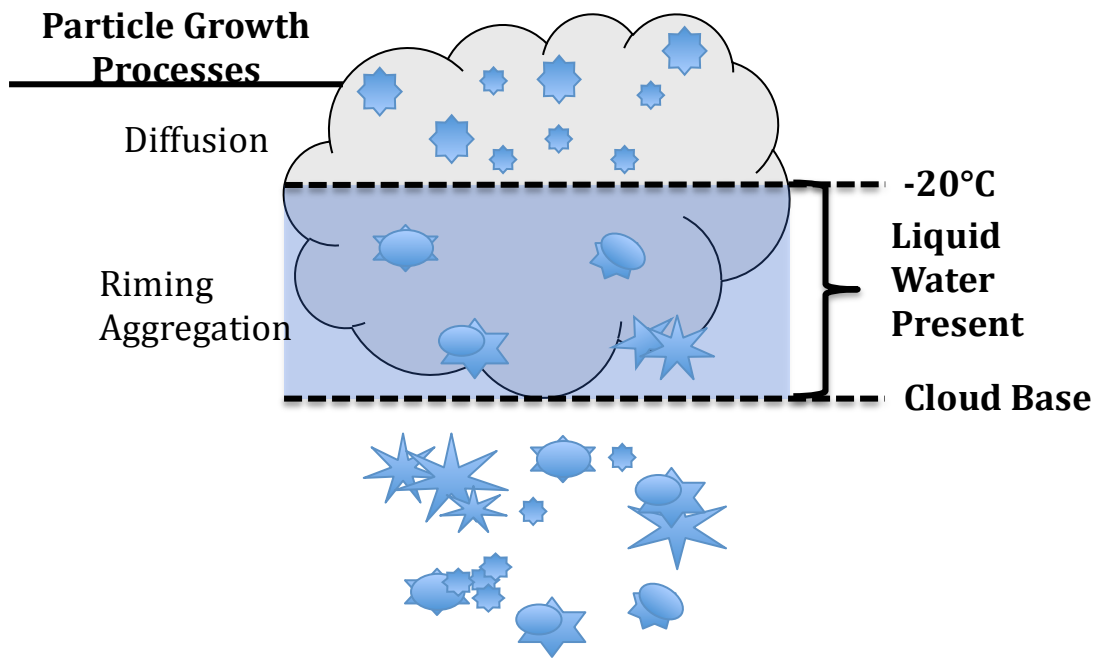
Figure 9 is a schematic that introduces snowflake growth processes. Particles growing by diffusion (top of diagram) will have delicate branching structures (and a number of other habits). Around -20°C liquid water can be present in a cloud (blue shading), where riming and aggregation can occur. In a system where all three processes occur, a variety of irregular snowflake shapes are produced (bottom of diagram).

Early in diffusive particle growth, water vapor diffuses short distances

through a cloud towards an ice particle and deposits on the surface. Intricate crystal

patterns can develop during growth, as branches are added and interconnected over

time. As particles continue to grow it takes more mass to increase the size of a

particle, which translates to a decrease in the rate at which a particle's maximum

linear diameter (or particle size) increases. Therefore, snowflakes that grow only by

diffusion will be constrained within a specific time-dependent size range. Consider

a hypothetical scenario where all ice particles in a system begin growing by

diffusion at the same time; once precipitation begins the particle masses will be

centered around a mean, resembling a Gaussian distribution. In reality, ice particle growth is initiated throughout the lifetime of a cloud, which contributes to the large number of small particles required to create an exponential distribution. In order to classify a distribution as exponential particles much larger than the mean must exist, but we mentioned that the largest particles grown by diffusion are grouped around a mean value. As our hypothesis suggests, this physical evidence implies that particles growing by diffusion will populate a PSD with a log-normal shape.

Riming is a growth process where liquid water adheres to the surface of an ice particle and freezes, obscuring intricacies within a growing crystal. In a system where riming dominates, conical 'graupel' particles are abundant within the crystal population. This process may contribute to PSD shape, but all particles analyzed from the Boulder deployment contained some degree of riming. Therefore in our study we are not able to determine the impact of riming on distribution shape.

Aggregation is the process of snowflake growth through collision and cohesion of multiple particles. Despite what Figure 9 suggests, liquid water is not mandatory for aggregation to occur. Ice particles created by this process are irregularly shaped because particles of any size or shape join together with little preference for orientation. As snowflakes continue grow in this system, they are more likely to collide with other particles resulting in a higher probability for aggregation. Therefore, ice particles grown in an aggregation dominant system are more likely to fit in an exponential distribution with many small particles and few very large particles.

CHAPTER 5

Results

5.1 Separating zero-stage from multi-stage aggregates

During visual inspection, particles were separated into two categories defined by aggregation state. Snowflakes classified as zero-stage aggregates (Figure 10.A) show no visual evidence of aggregation; 589 particles from the Boulder data set were placed in this category. The remaining 763 snowflakes were categorized as multi-stage aggregates (Figure 10.B). The software organizes analyzed snowflakes in a time ordered array, making it easy to separate snowflakes and analyze relationships between any parameters listed in Figure 3.
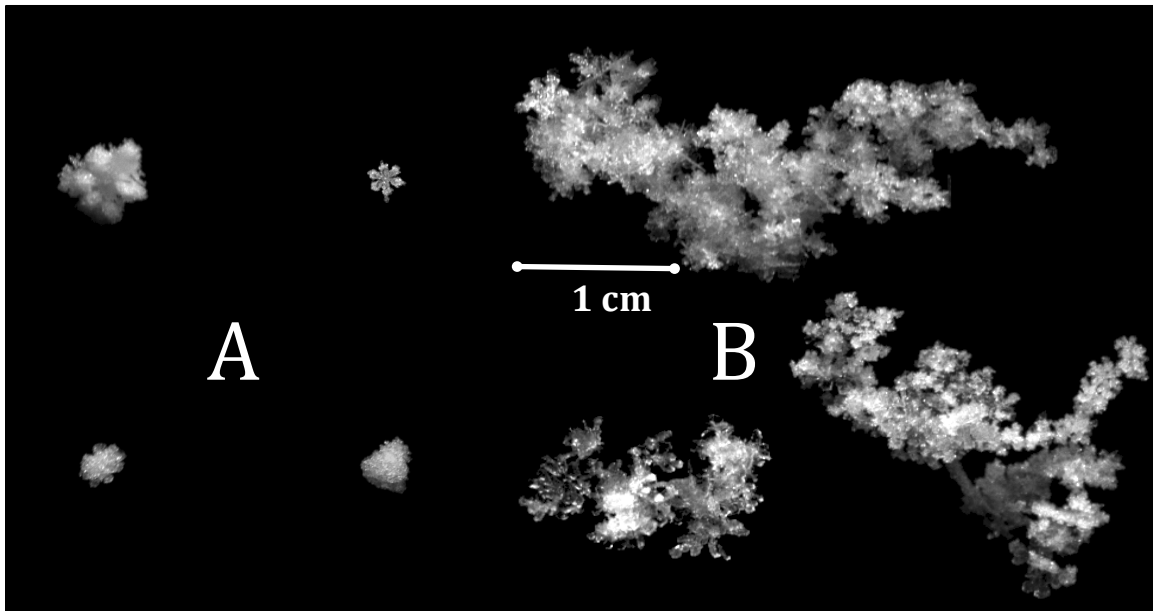
Figure 10 presents examples of multi-stage(B) and zero-stage aggregates(A). Not all multi-stage aggregates are this large or complex, but these examples show the variability in aggregate shapes. Most of the zero-stage aggregate particles look very similar to the ones presented.

The two distributions shown in Figure 11 provide evidence that the two distributions are separate. These histograms are not plotted on a semi-log scale, in order to preserve information about the tails of the distributions. Notice that the zero-stage distribution appears to be distributed evenly around 2000 microns (2 mm) while the tail of the multi-stage distribution extends far past the mean.
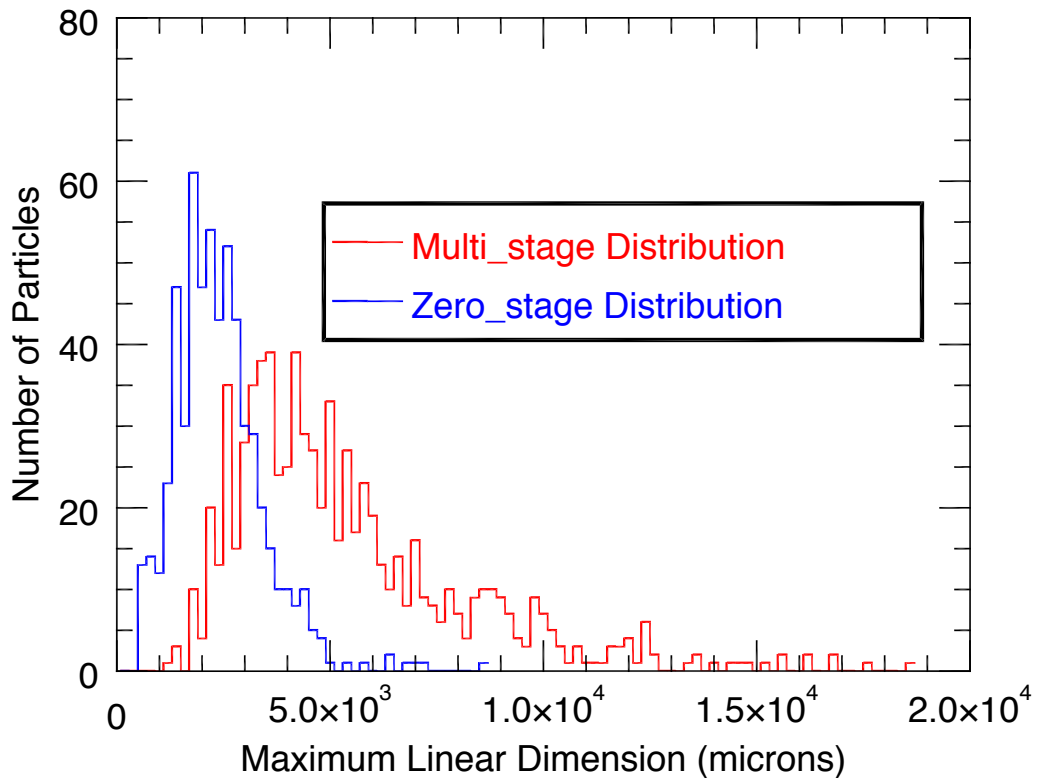

Figure 11 is a histogram of *Rmax* for the two aggregate state distributions. Notice that to first order, particle size segregates the two states efficiently. The tails of each distribution are very different, which encourages us to investigate PSD shape.

5.2 Size distributions of different aggregates

Before looking further into distributions of particles segregated by aggregation state, we will provide evidence for the first part of our hypothesis by looking at how our combined PSD deviates from a purely exponential distribution. The combined distribution contains all snowflakes analyzed during the Boulder field

campaign. Figure 12 is the observed combined PSD with a theoretical exponential

distribution plotted in black (9).

(9) $$Log(N_D) = 4179 - 0.002863 * D_{LE}$$

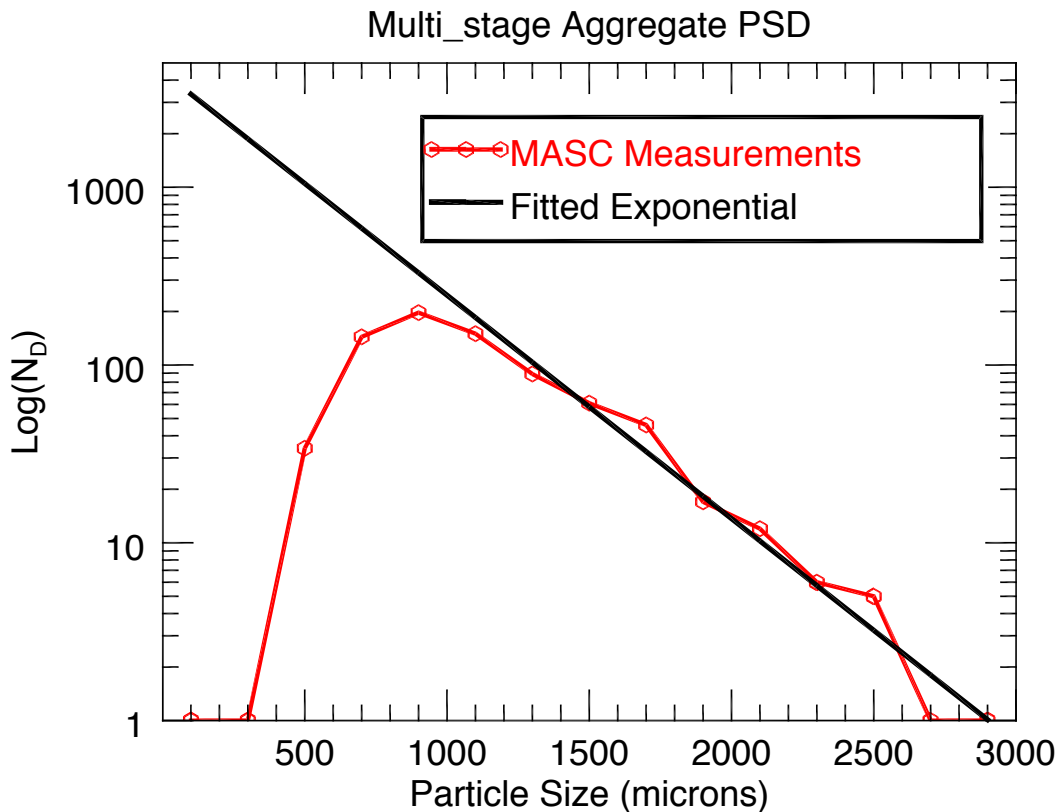### Combined Aggregate state PSD
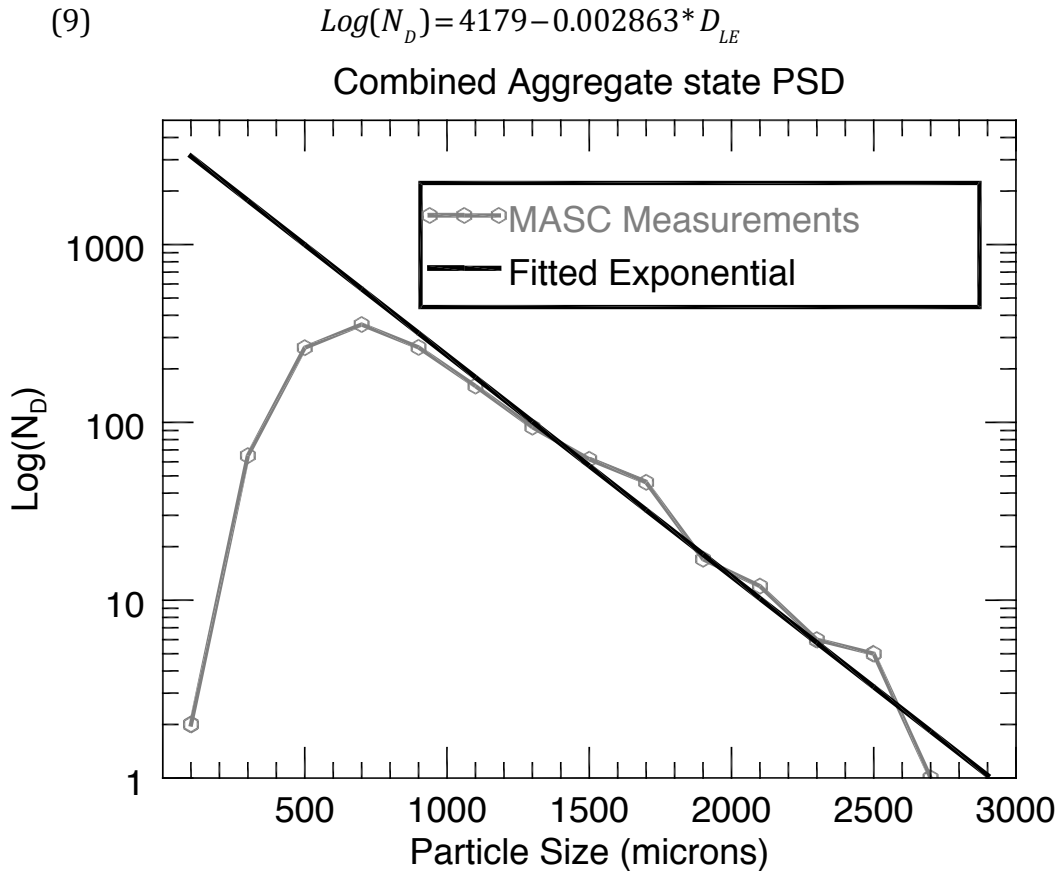
Figure 12 is the PSD for the combined distribution of MASC observations with a theoretical exponential distribution fitted where particle size is reported in D_{LE}. The theoretical distribution does not use particles smaller than 700 microns because they do not contribute to the exponential behavior of the system.

In Figure 12, the observations and theoretical distribution begin separating

for particles with liquid equivalent diameter around 7 mm. If the underlying

theoretical distribution is indeed exponential, then we are heavily under sampling

small particles with our software. To some extent, the software does favor large

over very small particles since they have more reasonable sharpness factors and

really small particles are fuzzy in raw MASC images. We do not believe that this

accounts for all of the discrepancy because particles with diameter between 5 and 7 mm (where the theoretical discrepancy is initiated) are too large to avoid detection by our software. Therefore we investigate how aggregation states separately contribute to the combined distribution to determine if it is purely exponential.

The multi-stage aggregate PSD (Figure 13) looks very similar to the combined PSD, but observations of particles less than 9000 microns are significantly lower. The theoretical exponential distribution (10) has a decay rate (or slope) that is very similar to the combined PSD.
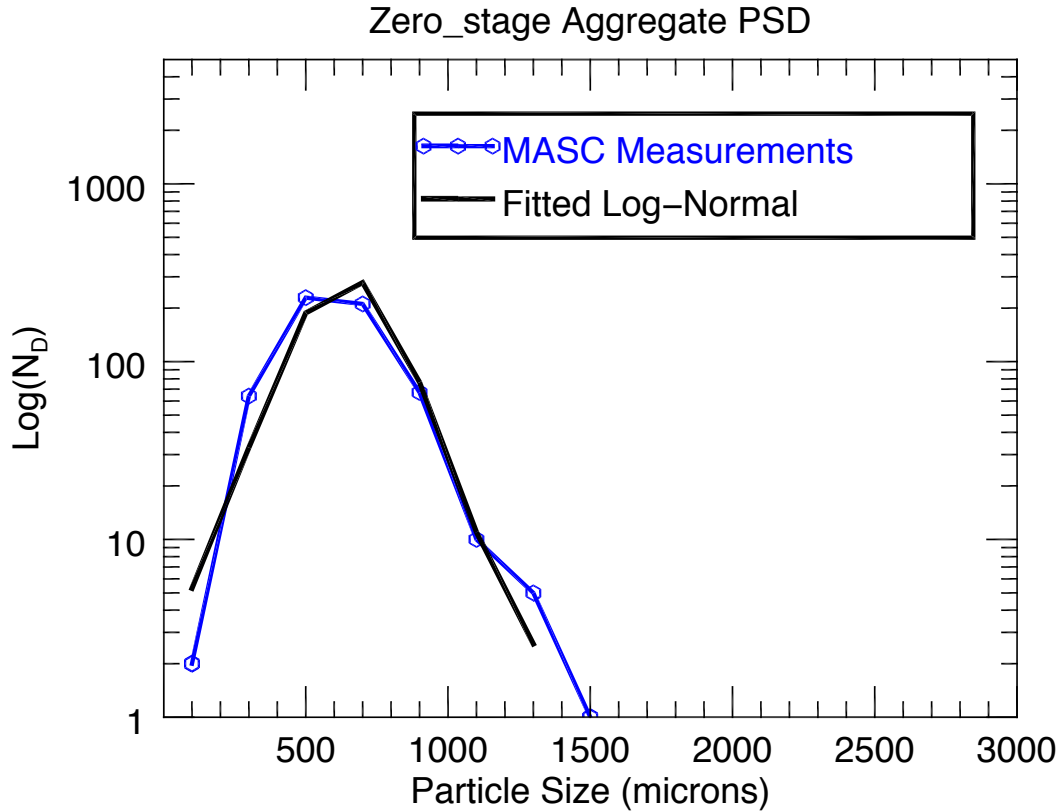
$$(10) \qquad Log(N_D) = 4458.7 - 0.002893 * D_{LE}$$

Figure 13 is the PSD for the multi-stage distribution of MASC observations with a theoretical exponential distribution fitted where particle size is reported in D_{LE}. Notice that the distribution between 300 and 1000 microns falls faster than the combined distribution.

This distribution also fails to adhere strictly to an exponential distribution for small particle size, but we expect these particles to exhibit such behavior. In order to be visually categorized as multi-stage aggregates, the two particles need to be large enough to be distinguishable from each other making smaller particles less likely to be recognized as multi-stage. In addition, riming can obscure very small multi-stage aggregates, which can explain some deviation from exponential behavior.

The zero-stage aggregate PSD (Figure 14) is very different from other distributions that we have presented. The limbs on either side of the distribution mode are even and appear to be similarly spaced, which suggests a log-normal distribution when we consider that this plot is on semi-log axes (11).
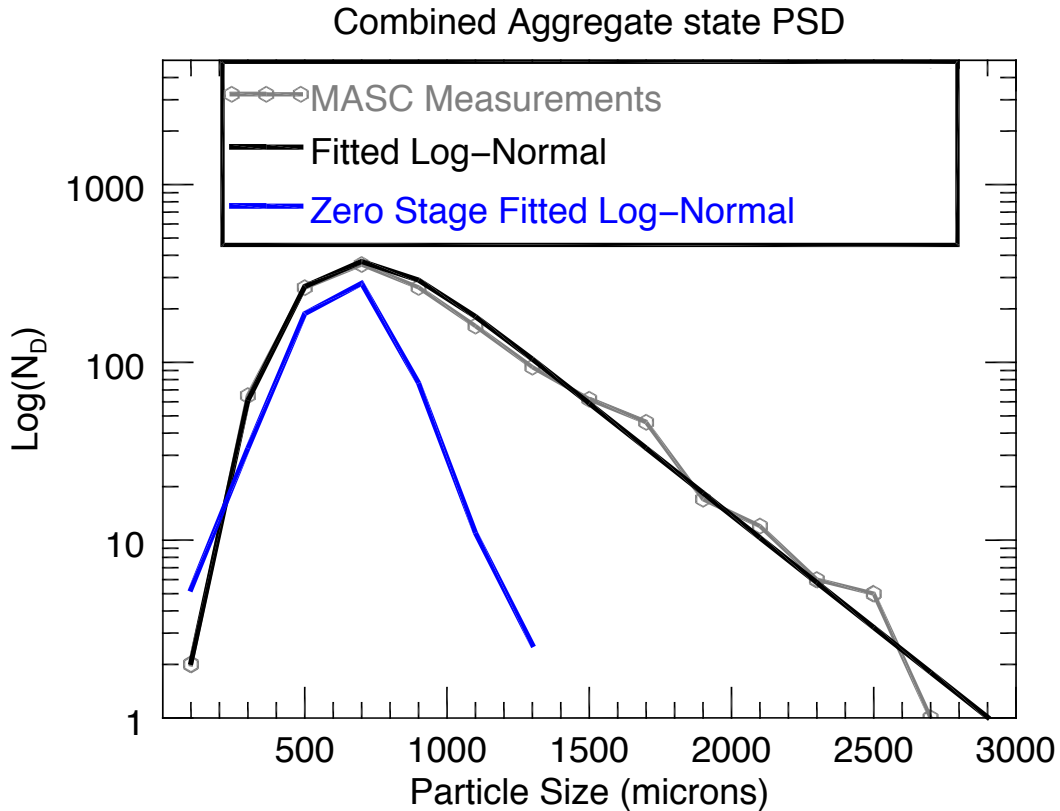
(11)
$$Log(N_D) = 5.70e^{\frac{-z^2}{2}}$$
$$z = \frac{D_{LE} - 643.5}{346.7}$$

Figure 14 is the PSD for the zero-stage distribution of MASC observations with a theoretical log-normal distribution fitted where particle size is reported in D_{LE}. The termination of both tails is good evidence that an exponential distribution will not fit these observations.

Because the combined distribution encompasses both aggregation state distributions, we calculated a theoretical distribution that is a log-normal distribution with an exponential influence in the right tail (12) (Figure 15). We need more snowfall observations before we can determine physical relationships between this equation and atmospheric conditions.

$$(12) \quad Log(N_D) = -40.8e^{\frac{-z^2}{2}} + 8.43 - 0.002904 * D_{LE}$$
$$z = \frac{D_{LE} + 880.8}{531.2}$$

Figure 15 is the PSD for the combined distribution of MASC observations with a unique theoretical distribution fitted where particle size is reported in D_{LE}. The distribution is lognormal for small particle sizes and has an exponential tail as size increases. The zero-stage distribution is plotted as well to lend perspective to how the new distribution looks compared to a purely lognormal distribution.

5.3 Comparison with existing size distributions

To confirm our results, we compare the slopes of MASC exponential

distributions to published PSDs. *Braham* [1990] collected 19 particle size data of

frozen precipitation using a particle measuring probe mounted to a research

aircraft; the data was subsequently plotted by *Matrosov* [2007]and are shown as

black lines in Figures 16 and 17. *Sekhon and Srivastava* [1970] defined theoretical

relationships for PSDs that vary based on precipitation rate (R). (5)-(8)
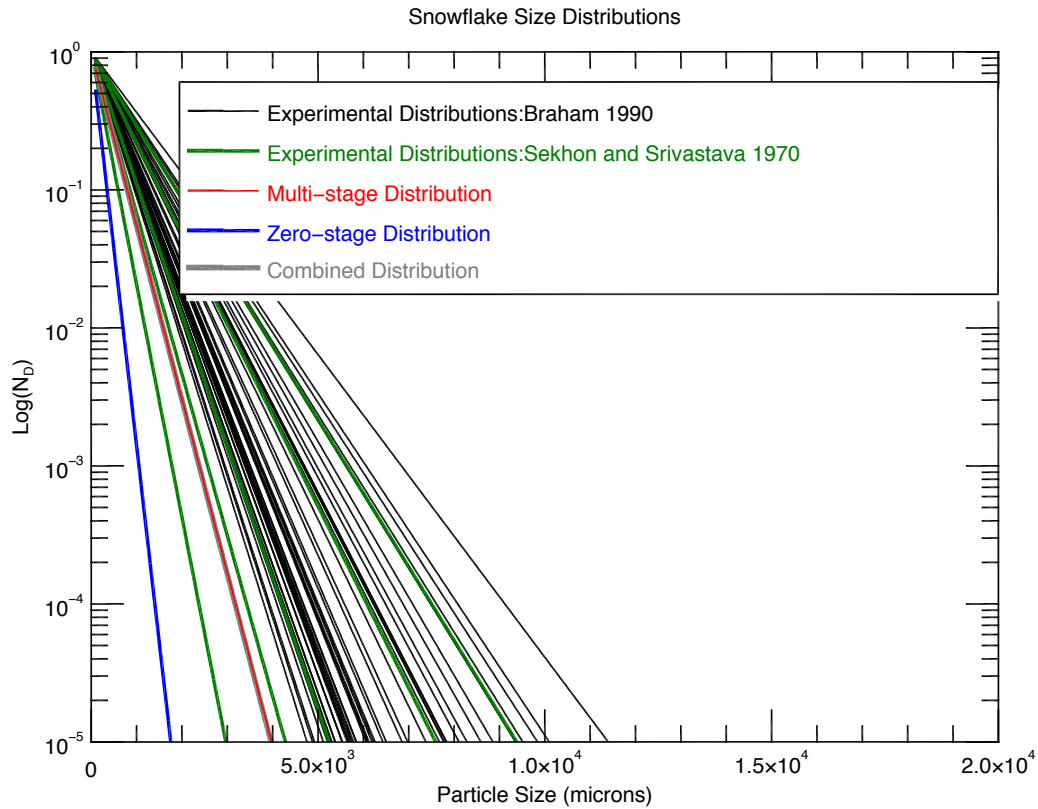
Figure 16 compares the slopes of distribution from three different studies. The black lines are the 19 distributions collected by [*Braham*, 1990] while the green lines are theoretical distributions calculated by [*Sekhon and Srivastava*, 1970] that depend on precipitation rate. Our observations are presented in red, gray and blue. The zero-stage distribution was calculated with the same method as the other two distributions.
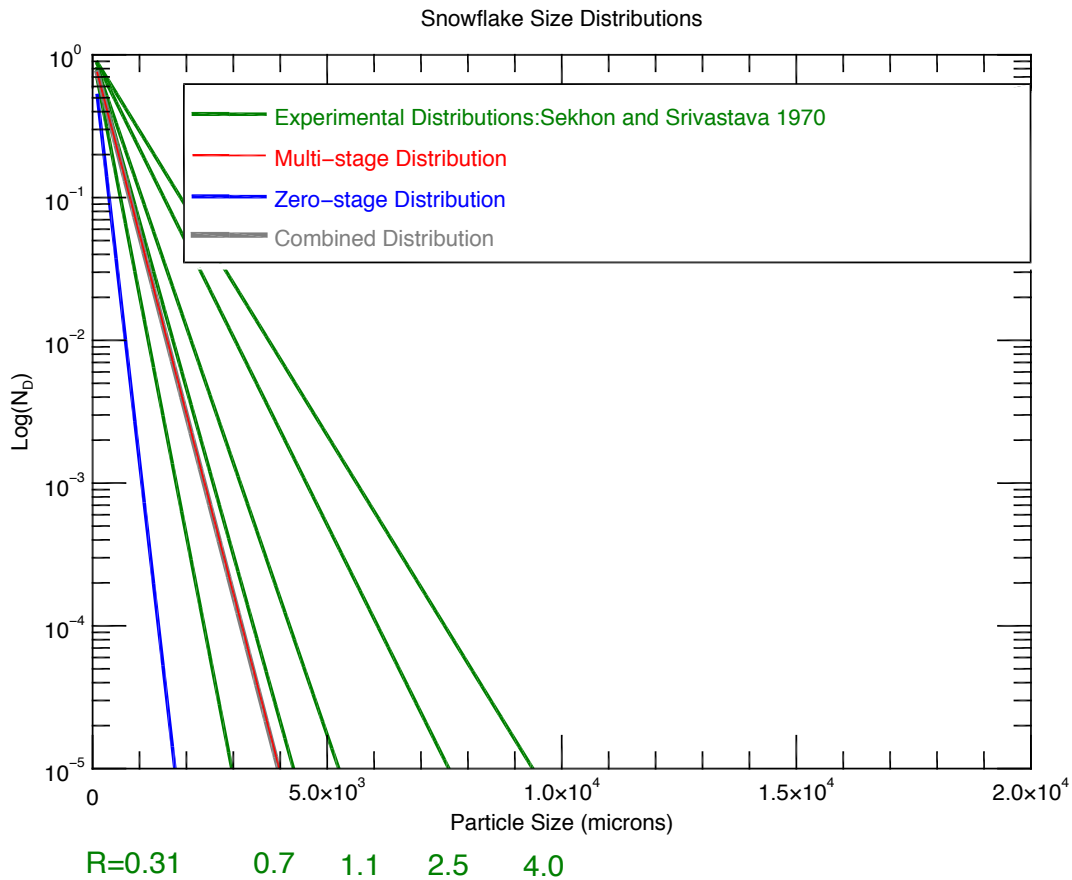
Figure 17 is identical to Figure 16, but the black distributions were removed to make comparisons easier. Notice that the red and gray distributions are almost identical which makes them difficult to distinguish.

Our multi-stage and combined distributions have slopes that fit within the range of PSDs observed or calculated between the two studies, while an exponential 'fit' on the zero-stage distribution does not. The disagreement between our zero-stage exponential fit and the other distributions is encouraging, since we do not present this distribution as exponential.

CHAPTER 6

Conclusions

During analysis of snowfall in Colorado, we found evidence that Particle Size Distributions are not strictly exponential. Using software we developed for the MASC, we measured particle information for snowflakes from 1500 image triplets. We then visually segregated particles by aggregation state and create PSDs to observe the distribution behavior. We hypothesize that particle growth processes impose physical limitations on distributions of particles. Most importantly, particles grown by diffusion only will not be able to grow large enough to enable an exponential size distribution. Aggregation is a process where the rate of growth is controlled by the number of collisions a particle experiences, therefore large particles grow faster than smaller particles during aggregation. Here we present evidence that the distribution of falling snowflakes may indeed be a combined distribution composed of log-normal (non-aggregates) and exponential (aggregates) distributions.

In order to further validate these findings and create a more robust dataset, we will collect images from the MASC while it is deployed in Summit, Greenland and Marquette, Michigan. By gathering information from different locations, we will determine how distributions are affected by parameters such as temperature and presence of liquid water. In addition, while the MASC is in Greenland it will be co-located with vertically pointing radar. This allows us to directly compare

reflectivity profiles to snowfall measurements in an attempt to address radar

retrieval uncertainty.

REFERENCES

Braham, R. R. (1990), Snow Particle Size Spectra in Lake Effect Snows, *Journal of Applied Meteorology*, *29*, 8.

Ewert, H., A. Groh, and R. Dietrich (2012), Volume and mass changes of the Greenland ice sheet inferred from ICESat and GRACE, *Journal of Geodynamics*, *59-60*, 13.

Garrett, T. J., E. H. Bair, C. J. Fallgatter, K. Shkurko, R. E. Davis, and D. Howlett (2012), The Multi-Angle Snowflake Camera, *2012 International Snow Science Workshop*, 4.

Gunn, K. L. S., and J. S. Marshall (1958), The distribution with size of aggregate snowflakes, *Journal of Meteorology*, *15*, 10.

Howat, I. M., Y. Ahn, I. Joughin, M. R. van den Broeke, J. T. M. Lenaerts, and B. Smith (2011), Mass balance of Greenland's three largest outlet glaciers, 2000-2010, *Geophysical research letters*, *38*, 5.

Kajikawa, M., and A. J. Heymsfield (1989), Aggregation of Ice Crystals in Cirrus, *Journal of the Atmospheric Sciences*, *46*(20), 14.

Kneifel, S., M. S. Kulie, and R. Bennartz (2011), A triple-frequency approach to retrieve microphysical snowfall parameters, *Journal of Geophysical Research*, *116*(D11), doi:10.1029/2010jd015430.

Krabill, W., et al. (2004), Greenland Ice Sheet: Increased coastal thinning, *Geophysical research letters*, *31*, 4.

Kulie, M. S., R. Bennartz, T. J. Greenwald, Y. Chen, and F. Weng (2010), Uncertainties in Microwave Properties of Frozen Precipitation: Implications for Remote Sensing and Data Assimilation, *Journal of the Atmospheric Sciences*, *67*(11), 3471-3487, doi:10.1175/2010jas3520.1.

Kulie, M. S., M. J. Hiley, R. Bennartz, S. Kneifel, and S. Tanelli (2013), Triple-Frequency Radar Reflectivity Signatures of Snow: Observations and Comparisons with Theoretical Ice Particle Scattering Models, *Journal of Applied Meteorology and Climatology*, *53*, 19.

Marshall, J. S., and W. M. Palmer (1948), Shorter Contributions: The Distribution of Raindrops with Size, *Journal of Meteorology*, *5*, 2.

Matrosov, S. Y. (2007), Modeling Backscatter Properties of Snowfall at Millimeter Wavelengths, *Journal of the Atmospheric Sciences*, *64*, 10.

Nowell, H., G. Liu, and R. Honeyager (2013), Modeling the microwave single-scattering properties of aggregate snowflakes, *Journal of Geophysical Research: Atmospheres*, *118*, 13.

Pritchard, H. D., R. J. Arthern, D. G. Vaughan, and L. A. Edwards (2009), Extensive dynamic thinning on the margins of the Greenland and Antarctic ice sheets, *Nature*, *461*, 5, doi:10.1038/nature08471.

Rignot, E., J. L. Bamber, M. R. van den Broeke, C. Davis, Y. Li, W. Van de Berg, and E. Van Meijgaard (2008), Recent Antarctic ice mass loss from radar interferometry and regional climate modelling, *nature geoscience*, *1*, 5.

Rignot, E., I. Velicogna, M. R. van den Broeke, A. Monaghan, and J. T. M. Lenaerts (2011), Acceleration of the contribution of the Greenland and Antarctic ice sheets to sea level rise, *Geophysical research letters*, *38*, 5, doi:10.1029/2011GL046583.

Sasgen, I., M. R. van den Broeke, J. L. bamber, E. Rignot, L. S. Sorensen, B. Wouters, Z. Martinec, I. Velicogna, and S. B. Simonsen (2012), Timing and origin of recent regional ice-mass loss in Greenland, *Earth and Planetary Science Letters*, *333-334*, 11.

Sekhon, R. S., and R. C. Srivastava (1970), Snow Size Spectra and Radar Reflectivity, *Journal of the Atmospheric Sciences*, *27*, 9.

Seliga, T. A., and V. N. Bringi (1976), Potential Use of Radar Differential Reflectivity Measurements at Orthogonal Polarizations for Measuring Precipitation, *Journal of Applied Meteorology*, *15*, 8.

van den Broeke, M. R., J. Bamber, J. Ettema, E. Rignot, E. Schrama, W. J. van de Berg, E. van Meijgaard, I. Velicogna, and B. Wouters (2009), Partitioning Greenland Mass Loss, *Science*, *326*, 4.

van den Broeke, M. R., J. Bamber, J. Lenaerts, and E. Rignot (2011), Ice Sheets and Sea Level: Thinking Outside the Box, *Surveys of Geophysics*, *32*, 11, doi:10.1007/s10712-011-9137-z.

Vaughan, D. G., et al. (2013), Observations: Cryosphere. In: Climate Change 2013: The Physical Science Basis. Contribution of Working Group I to the Fifth Assessment Report of th Intergovernmental Panel on Climate Change.